Simulation Framework and Case Studies for the Design of Sea Surface Salinity Remote Sensing Missions

Alexander Akins, *Member, IEEE*, Shannon Brown, *Senior Member, IEEE*, Tong Lee,
Sidharth Misra, *Senior Member, IEEE*, and Simon Yueh, *Fellow, IEEE*

***Abstract*—*L*-band microwave radiometers have now been used to measure sea surface salinity (SSS) from space for over a decade with the SMOS, Aquarius, and SMAP missions, and it is expected that the launch of the CIMR mission in the later half of this decade will ensure measurement continuity in the near future. Beyond these missions, it is useful to consider how future missions can be designed to meet different scientific objectives and performance requirements as well as to fit within different cost spaces. In this article, we present a software simulator for remote sensing measurements of ocean state capable of generating L1- and L2- equivalent data products for an arbitrary spacecraft mission including multifrequency fixed-pointing or scanning microwave radiometers.This simulator is then applied to case studies of SSS measurement over selected areas of interest, including the Gulf Stream, Southern Ocean, and Pacific tropical instability wave regions. These simulations illustrate how different design choices concerning receiver bandwidth and revisit time can improve the detection of SSS features in these regions from the mesoscale to the seasonal scale.**

***Index Terms*—Microwave radiometry, ocean salinity, open source software.**

I. INTRODUCTION

As a result of decades of research, passive microwave radiometer instruments have been and continue to be used operationally to measure ocean state parameters with useful accuracy. While sea surface temperature (SST) and ocean vector winds (OVW) can be measured remotely through other means (e.g., scatterometers, infrared radiometers), sea surface salinity (SSS) in particular is primarily measured remotely by microwave radiometers operating at wavelengths longer than approximately 5 cm. Conventionally, *L*-band (1.4 GHz) radiometers are used to take advantage of the protected spectral window used by radio astronomers to study galactic emission near the 21 cm hydrogen line. While the SSS signal is stronger at lower frequencies, the prevalence of radio frequency interference (RFI) at these frequencies has limited SSS measurement efficacy in the past. *L*-band radiometers have served as the key instruments for the Soil Moisture and Ocean Salinity (SMOS), Aquarius/SAC-D, and Soil Moisture Active-Passive (SMAP) missions [1]. Both currently operational missions, SMOS and SMAP, are beyond their nominal lifetime, and they will remain the only missions capable of measuring SSS from space until the expected launch of both the ESA Copernicus Imaging Microwave Radiometer (CIMR) mission [2] and the Chinese Ocean Salinity Mission [3] in the coming years. Looking forward, it is highly desirable to improve the quality of retrieved ocean state parameters via novel observing systems. The crucial remaining issues for current SSS products are their poor accuracy at high latitudes [4], near land and sea ice edges, and over high wind regions. CIMR's multifrequency approach should permit the mitigation of sea ice and high wind effects. However, further enhancement to the CIMR design would allow more sensitive detection of salinity changes at high latitudes. Both NASA and ESA/CNES-funded study teams are working to refine concepts that could enable SSS remote sensing at higher resolution (such as SMOS-HR, [5]) and with greater sensitivity (such as UWBRAD, [6]). The use of a broadband radiometer system is particularly interesting due to its potential to significantly reduce the dependence of SSS retrievals on accurate ancillary data [6] and increased sensitivity to SSS in general [7]. While broadband measurements have been conventionally limited by RFI, the recent CubeRRT mission has effectively demonstrated that RFI can be mitigated to great effect through the use of digital spectrometers with high spectral resolution [8]. While these studies have provided encouraging results, there remains no solid path forward for SSS remote sensing from space beyond CIMR. It may also be necessary to design lower-cost missions with heritage technology that are capable of maintaining continuity in SSS measurements, which is necessary to ensure continued integration of SSS into climate forecasts. The minimization of spacecraft radiometer components could also enable the deployment of several satellites to obtain high revisit time at the cost of native spatial resolution. These recent advances, among other mission architecture choices, should be thoroughly considered during the development process for new missions.

Manuscript received 14 October 2022; revised 28 November 2022 and 19 December 2022; accepted 31 December 2022. Date of publication 5 January 2023; date of current version 20 January 2023. This work was supported by the NASA Physical Oceanography program (R&A task 80NM0018F0585) and conducted at the Jet Propulsion Laboratory, California Institute of Technology, under a contract with the National Aeronautics and Space Administration under Contract 80NM0018D0004. *(Corresponding author: Alexander Akins.)*

The authors are with the Jet Propulsion Laboratory, California Institute of Technology, Pasadena, CA 91109 USA (e-mail: Alexander.Akins@jpl.nasa.gov; shannon.t.brown@jpl.nasa.gov; tlee@jpl.nasa.gov; sidharth.misra@jpl.nasa.gov; simon.yueh@jpl.nasa.gov).

Digital Object Identifier 10.1109/JSTARS.2023.3234407

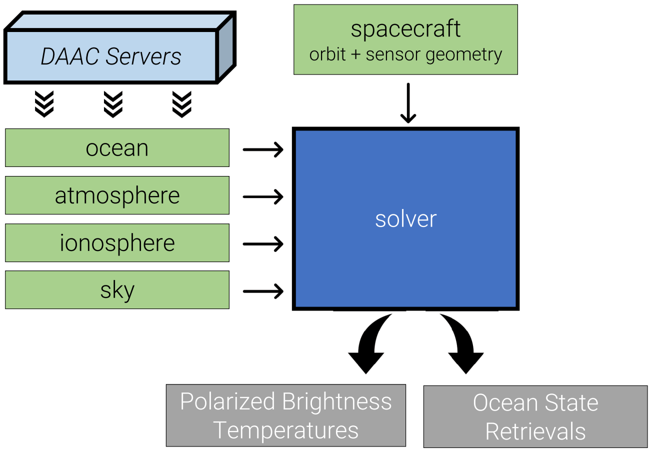

Fig. 1. Block diagram showing the module structure of the FOAM package.

In this article, we present a mission simulation software package focused on passive microwave measurements of ocean state. This simulator is capable of generating L1- and L2- equivalent data products for an arbitrary spacecraft mission including multifrequency fixed-pointing or scanning microwave radiometers. Following a detailed description of this simulator and its components, we then apply this tool to case studies of SSS retrievals over selected regions of broad oceanographic interest. Specifically, we simulate SSS measurements over the Gulf Stream, Southern Ocean, and Pacific tropical instability wave regions, investigating how different mission design choices affect the quality of the retrieved SSS over mid-, high-, and low-latitude oceans, respectively. These simulations underscore the utility of wideband radiometer architectures in future measurements of global SSS and the potential for less-capable missions to ensure continuity of measurement or to accommodate targeted revisit strategies.

II. MISSION SIMULATOR

To quickly investigate different mission architectures for ocean state parameter measurement, we have developed a mission simulator capable of generating L1 (brightness temperatures) and L2 (retrieved parameters) products for an arbitrary fixed-pointing or conically scanning passive microwave radiometer satellite mission geometry. Our mission simulator, which we call the forward ocean atmosphere microwave (FOAM) radiative transfer model,[1] is written in the Python programming language and has been developed to flexibly simulate the impact of mission design choices on the accuracy of ocean state parameter retrieval. As shown in Fig. 1, the FOAM package centers around the solver module, which combines inputs from several, independent geophysics modules to compute brightness temperatures (forward model, L1) and retrieve ocean state parameters (inverse model, L2). Each geophysics module reads ancillary data files provided by the user or downloads data from various distributed active archive centers (DAACs). In this section, the individual modules are described, as is the underlying remote sensing theory relevant to their use.

A. Spacecraft Module

FOAM's spacecraft module defines and simulates spacecraft orbits and radiometer measurement geometries The module can simultaneously accommodate heterogeneous constellations of spacecraft and is built around the SPICE toolkit [9], [10]. Spacecraft orbital parameters from two-line element sets are used to generate spacecraft SPICE kernels. Spacecraft clock kernels are defined with microsecond precision, which sets a lower limit for the allowable radiometer integration time (usually on the order of milliseconds to seconds). Any number of distinct radiometer instruments can be defined for a given spacecraft, and these radiometers can be defined either with fixed pointing or with fixed-speed scanning about an arbitrary axis. We note that the characteristics of the receiver backend (center frequency, bandwidth, noise temperature, integration time, etc.) are not specified here and instead are supplied to the solver module immediately prior to the brightness temperature calculation or model inversion. After the spacecraft and instruments are defined, they can be used to generate observations for a given time range and resolution. At present, antenna pattern integration is not included and the spatial resolution of the measurements is defined by the user-specified sampling/gridding resolution; the effect of antenna patterns will be incorporated in future updates to the simulator. The output of the observation generation routine includes the sample times, the latitude and longitude of the sampled location, the incidence angle and incidence azimuth, and the direction of specular reflection in the inertial frame. The spacecraft module includes utilities for computing revisit times for a given spacecraft or constellation, and predefined routines for generating spacecraft objects based on Aquarius and SMAP are also available.

All coordinate systems relevant to the FOAM package follow a right-handed convention. Those that are defined by the SPICE implementation are the inertial frame (J2000) and the body-fixed terrestrial reference frame (ITRF93). FOAM defines a topocentric reference frame with the x-axis looking east, the y-axis looking north, and the z-axis as the surface normal. This frame is aligned with the basis vectors for wind speed in the oceanographic convention provided by FOAM's default ancillary data files. Since the azimuthal dependence of wind-roughened ocean surface emission is commonly defined with $\phi = 0$ looking in the upwind direction, the azimuth angle for surface emissivity determination is defined as the difference between the wind direction vector and the incident azimuth in the topocentric frame. Finally, FOAM defines the spacecraft reference frame with the x-axis pointing toward the earth's center, the y-axis in the direction of the orbital velocity vector, and the z-axis perpendicular to the orbital velocity vector. Individual radiometer reference frames are defined as rotated modifications to this reference frame with a zero or nonzero angular velocity about one of those axes. The spacecraft and topocentric coordinate systems are illustrated in Fig. 2.

---

[1] FOAM is available publicly at https://github.com/jpl-microwave-instrument-science/foam

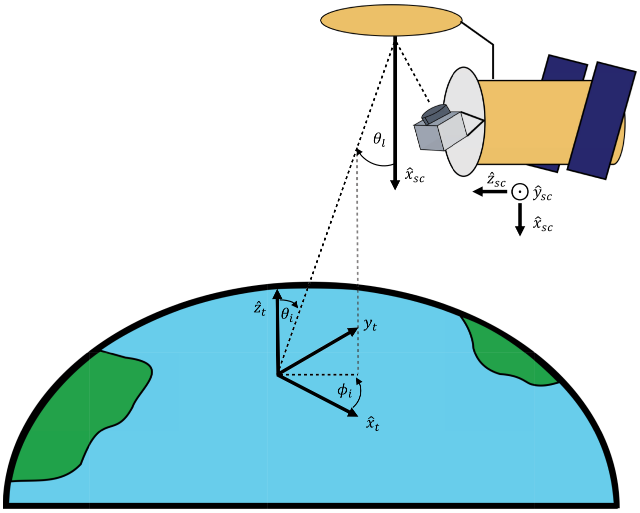

Fig. 2. Illustration of spacecraft and topocentric coordinate systems. The spacecraft coordinate frame is shown with the assumption that the orbital velocity vector points perpendicularly out of the page. The look angle θ_l is specified during radiometer definition and used to compute the incidence angle θ_i and incidence azimuth ϕ_i in the topocentric frame.

B. Ocean Module

FOAM's ocean module provides methods for computing emission and reflection from ocean surfaces as a function of temperature, salinity, and near-surface wind speed, which are three ocean-surface parameters that have major contributions to surface brightness temperature at lower frequencies. Before discussing this module, we define terms relevant to passive remote sensing of microwave radiation. Microwave radiometers measure the centimeter-wavelength radiance emitted by the ocean surface. This radiance can be expressed as a blackbody brightness temperature T_B through the Rayleigh–Jeans approximation to Planck's law. The polarization of microwave radiation can be described using the Stokes parameters $[I, Q, U, V]$ (or Stokes vector I_s) [11]. These parameters can also be written as brightness temperatures measured by linearly polarized instruments $[T_V, T_H, U, V]$, where $I = T_V + T_H$ and $Q = T_V - T_H$ and V and H subscripts describe linear vertical and horizontal polarizations. In both forms, the first two Stokes parameters describe the radiance measured by radiometers in each polarization, and the second two (U, V) describe the correlation of the field strength between polarizations.

For a radiometer viewing a specular ocean surface, there is no correlation between fields with different polarizations, so $U = V = 0$. Due to the high loss characteristics of salt water at microwave frequencies, the specular ocean surface can be described as single-layer, homogeneous medium. The brightness temperature of the specular ocean at an incidence angle θ_i is the product of the sea surface temperature T_S and the ocean emissivity ϵ (also shown below in terms of reflectivity R_p, where p is either V or H depending on polarization). The emissivity and reflectivity of the ocean surface are determined by the dielectric constant ε of the water

$$T_B = \epsilon T_S = (1 - R_p) T_S \tag{1}$$

$$R_V = \left(\frac{\varepsilon \cos\theta - \sqrt{\varepsilon - \sin^2\theta}}{\varepsilon \cos\theta + \sqrt{\varepsilon - \sin^2\theta}} \right)^2 \tag{2}$$

$$R_H = \left(\frac{\cos\theta - \sqrt{\varepsilon - \sin^2\theta}}{\cos\theta + \sqrt{\varepsilon - \sin^2\theta}} \right)^2 .$$

The dielectric constant of water varies as a function of frequency, salinity, and water temperature. FOAM's default dielectric model for salt water is that of Klein and Swift [12], which is a Debye relaxation model fit to low frequency laboratory measurements. The Debye relaxation model is written in terms of the angular frequency $\omega = 2\pi f$, the vacuum permittivity ε_0, a relaxation parameter τ, conductivity σ, and low frequency and high frequency dielectric constants ε_s and ε_∞.

$$\varepsilon = \varepsilon_\infty + \frac{\varepsilon_s - \varepsilon_\infty}{1 + (j\omega\tau)^{1-\alpha}} - j\frac{\sigma}{\omega\varepsilon_0}. \tag{3}$$

While the expression of Klein and Swift [12] has been used for many years, modeling of the dielectric constant of salt water remains an active subject of research. In addition to the Klein and Swift [12] model, FOAM's dielectric module also implements the models of Ellison [13] and the GW model [14], which are derived from laboratory measurements, and the models of Meissner and Wentz [15], [16], and Boutin et al. [17], which have been tuned to match Special Sensor Microwave/Imager (SSM/I) and SMOS observations from space. Fig. 3 illustrates the differences between dielectric constants predicted by these models from 1 to 40 GHz. Since many other dielectric constant models exist in literature, FOAM allows the user to provide their own models as function arguments to ocean objects.

In addition to the dielectric constant of salt water, the emissivity of the ocean is also governed by the roughness of its surface. The friction between near-surface winds and the ocean surface induces wind waves, and the impact of these waves on emissivity can be parameterized using surface roughness models. FOAM implements both empirical and theoretical models for the relationship between near-surface winds, ocean surface roughness, and ocean surface emissivity.

1) Empirical Models: Empirical geophysical model functions (GMFs) for ocean surface wind-roughening are developed for measurements at a single frequency based on match-up comparisons between radiometer measurements and ground-truth wind speed measurements acquired via other means. Match-ups are used to determine the values of coefficients A_n for a harmonic series augmentation to the specular emissivity [16], [18], [19]. Again, the azimuth direction ϕ is the difference between the topocentric wind azimuth direction and the radiometer azimuth look direction, where $\phi = 0$ looks upwind

$$\epsilon_{[p=T_V, T_H]} = \epsilon_0 + \sum_{n=0}^{N} A_n^p \cos(n\phi) \tag{4}$$

$$\epsilon_{[p=U,V]} = \sum_{n=0}^{N} A_n^p \sin(n\phi). \tag{5}$$

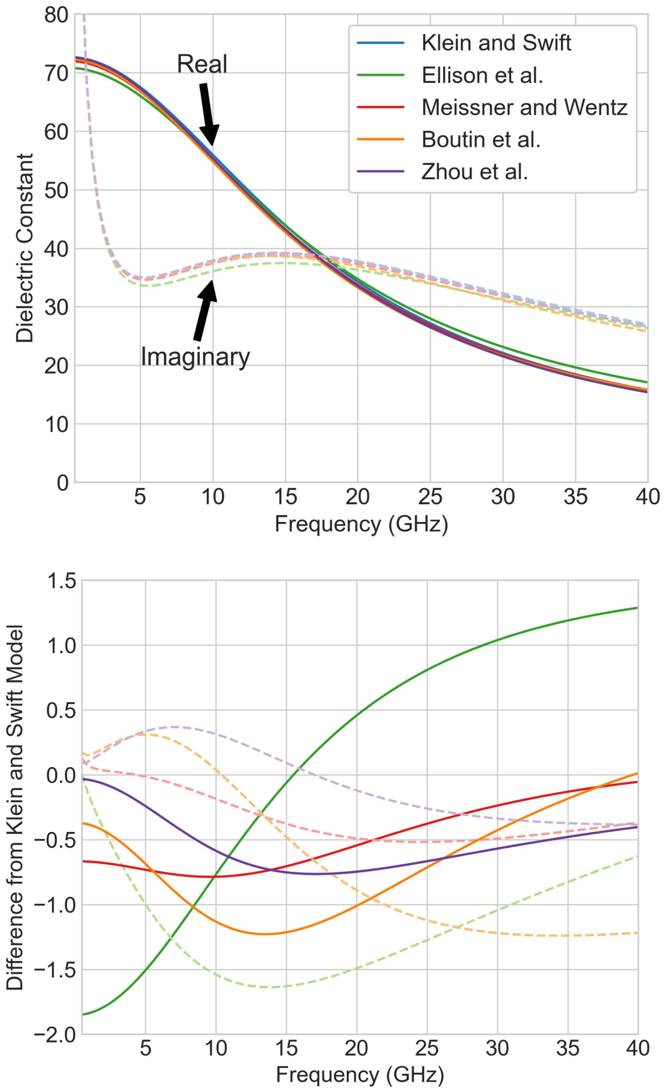

Fig. 3. Comparison between real and imaginary dielectric constant models included with FOAM. Dielectric constant models are shown for SST = 20 °C and SSS = 34 psu.

FOAM implements the GMFs of Meissner and Wentz [16], [18] at 1.4, 6.8, 10.7, 18.7, and 37 GHz, which were developed by comparing Aquarius, WindSat, and SSM/I observations with independent wind speed measurements. FOAM interpolates and extrapolates the wind-dependence coefficients of these GMFs from 0 to 40 GHz (with specular emissivity assumed at the static limit). These models provide reasonable accuracy over this range at low computation expense.

2) Theoretical Models: Theoretical models of ocean surface roughening consider roughness-dependent emission mechanisms on multiple scales, and FOAM implements the two-scale surface roughness model of Yueh [20]. Two-scale ocean roughness models treat emission from ocean surfaces roughened by large-scale gravity waves using a geometric optics approach wherein the ocean surface is modeled as a collection of tiles with tilt slopes S. The expression below separates the slopes in the local topographic x and y vector directions, although it could also be formulated in terms of the upwind S_u and cross-wind S_c directions. Shadowing is taken into account in the integration limit of the S_x term [20]

$$T_p = \int_{-\infty}^{\infty}\int_{-\infty}^{\cot(\theta)} I_s(1 - S_x\tan(\theta))P(S_x, S_y)dS_x dS_y. \quad (6)$$

The slope probability distribution $P(S_x, S_y)$ is assumed to be zero-mean Gaussian with variances determined by the surface spectrum $W(\kappa, \phi)$

$$P(S_x, S_y) = \frac{1}{2\pi\sigma_x\sigma_y}e^{-\frac{1}{2}\left(\frac{x^2}{\sigma_x^2}+\frac{y^2}{\sigma_y^2}\right)} \quad (7)$$

$$\sigma_x^2 = \int_{\infty}^{\infty}\int_0^{2\pi} \kappa^3\cos^2(\phi)W_l(\kappa, \phi)d\phi dk$$

$$\sigma_y^2 = \int_{\infty}^{\infty}\int_0^{2\pi} \kappa^3\sin^2(\phi)W_l(\kappa, \phi)d\phi dk.$$

The ocean surface spectrum $W(\kappa, \phi)$ describes the distribution of ocean surface wave energy as a function of the wavenumber κ [21]. Since this spectrum is generally a continuous function, two-scale models divide the spectrum into large and small scale components by selecting a two-scale cutoff wavenumber κ_d. The value of κ_d can vary, and is generally selected to be less than the electromagnetic wavenumber by a factor between 3 and 5. [20]. The large-scale surface spectrum $W_l(\kappa, \phi)$ is equivalent to $W(\kappa, \phi)$ up to $\kappa = \kappa_d$, and it is zero beyond this wavenumber. The small-scale spectrum $W_s(\kappa, \phi)$ exhibits the opposite behavior. The spectrum $W(\kappa, \phi)$ is composed of an isotropic term $S(\kappa)$ and an anisotropic term $\Phi(\kappa, \phi)$

$$W(\kappa, \phi) = \frac{1}{2\pi\kappa}S(\kappa)\Phi(\kappa, \phi). \quad (8)$$

FOAM includes several different models for the isotropic spectrum, all of which are discussed in the appendix of Hwang [22] with the exception of the Durden and Vesecky [23] spectrum. For simplicity, FOAM assumes that ocean wave generation is not fetch-limited. The fetch dependence of several of the Hwang [22] expressions is eliminated by assuming a peak spectral frequency equivalent to that of the fully developed Pierson and Moskowitz spectrum. As shown in Fig. 4, the ocean spectrum models exhibit different spectral slopes, and the slope of the Hwang [22] general model can be modified via input arguments. The anisotropic component of the surface spectrum follows the form of Fung and Lee [24] and is shown below. The definition of c in the following expression is that of Yueh [20] and $s = 1.5 \times 10^{-4}$:

$$\Phi(k, \phi) = 1 + c(1 - e^{-s\kappa^2})\cos(2\phi). \quad (9)$$

These equations above describe roughened ocean surface emission in the large-scale sense. Each specular tile in the geometric optics expression also exhibits small-scale roughness and is partially covered with ocean foam. The Stokes vector of emission from a single tile I_s is a combination of emission from a foam-free roughened tile I_{ss} and emission from a foam-covered flat tile I_{sf}. The fraction of the surface element covered by foam

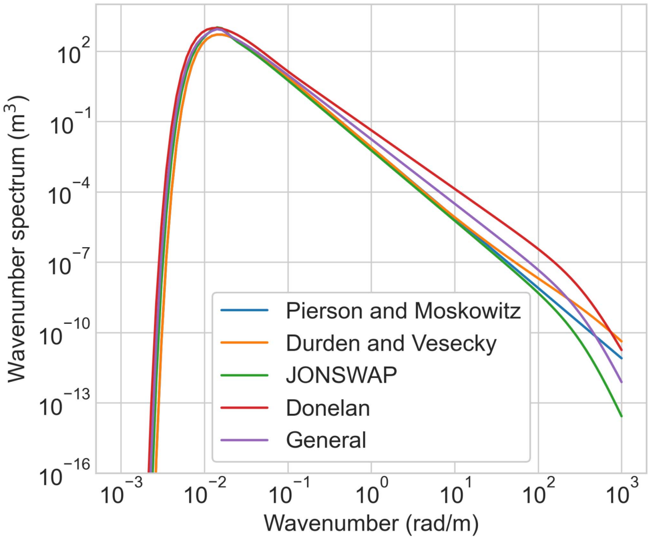

Fig. 4. Ocean spectrum models included in FOAM as discussed by [22]. Spectra are shown for a wind speed of 20 m/s.

is denoted F

$$I_s = (1 - F)I_{ss} + FI_{sf}. \tag{10}$$

FOAM uses the foam fraction expression of Hwang et al. [25], which is a function of wind friction u_*. This expression and the conversion between wind friction and 10-m wind speed u_{10} are both shown as follows:

$$F = \begin{cases} \max(0, 0.3(u_* - 0.11)^3) & u_* \leq 0.4\text{m/s} \\ 0.07u_*^{2.5} & u_* > 0.4\text{m/s} \end{cases} \tag{11}$$

$$u_* = u_{10}\sqrt{10^{-5}\left(-0.16u_{10}^2 + 9.67u_{10} + 80.58\right)}.$$

The Stokes vector of foam emission can be determined via (1) and (2) (and therefore no signature of U or V Stokes parameters is present) by using an effective dielectric constant for foam. FOAM uses a quadratic mixing rule between water (ε_w) and air ($\varepsilon_a = 1$) to estimate the dielectric constant of foam ε_f, following the suggestion of Anguelova [26]. FOAM's dielectric module also includes the foam dielectric constant model of Stogryn [27]

$$\varepsilon_f = \left(F\sqrt{\varepsilon_a} + (1 - F)\sqrt{\varepsilon_w}\right)^2. \tag{12}$$

The emission of foam-free surfaces with small scale roughness is described using a small perturbation method formulation for Bragg scattering. The resulting expression includes both coherent I_{coh} and incoherent I_{inc} terms

$$I_{ss} = T_S\left(\begin{bmatrix}1\\1\\0\\0\end{bmatrix} - (I_{coh} + I_{inc})\right)$$
$$= T_S\left(\begin{bmatrix}1 - R_V\\1 - R_H\\0\\0\end{bmatrix} - \int_0^\infty \int_0^{2\pi} \kappa W_s(\kappa, \phi)\begin{bmatrix}g_{T_V}\\g_{T_H}\\g_U\\g_V\end{bmatrix} d\phi d\kappa\right). \tag{13}$$

The small perturbation method solution method for small-scale rough surface emission (and scattering coefficients g above) are discussed at length by Yueh [20], [28] and Johnson [29], [30], and will not be repeated here. Surface roughness is also stronger on downwind large-scale tiles due to hydrodynamic modulation, so the small-scale emission is adjusted by an empirical scale factor as a function of the wave slope

$$W_s(\kappa, \phi) = hW_s(\kappa, \phi) \tag{14}$$

$$h = \begin{cases} 1 - 0.5\text{sign}(S_x) & \text{if}|S_x/S_u| > 1.25 \\ 1 - 0.4(S_x/S_u) & \text{if}|S_x/S_u| \leq 1.25. \end{cases}$$

Finally, a coordinate transformation from the topocentric system (where the z-axis points in the zenith direction) and the local wave system (where the z-axis points along the normal vector of a large-scale wave tile) is necessary to accurately compute the polarization of the emission and reflection [20]. In addition to including a full two-scale model, FOAM also includes the FASTEM-5 and FASTEM-6 ocean surface emissivity models which are empirical models fit to the output of similar full two-scale codes [31]. The main difference between the different FASTEM versions is the form of the azimuthal dependence.

Fig. 5 shows a comparison of ocean surface brightness temperature spectrum from 500 MHz to 40 GHz predicted by the empirical and two-scale surface models discussed above. Also shown in Figs. 6 and 7 are the elevation and azimuth dependence of T_p predicted by the models. For salinity remote sensing purposes, it is important to note that extrapolation of the FASTEM model to frequencies lower than 1.4 GHz results in nonphysical brightness temperature predictions, whereas the extrapolated Meissner–Wentz GMFs and the full two-scale model obtain reasonable agreement. Since the full two-scale model is computationally expensive in its current incarnation, it is recommended to use the MW GMF for low frequencies and the FASTEM model for high frequencies.

C. *Atmosphere Module*

FOAM's atmosphere module computes emission and attenuation from atmospheric gases and aerosols using both plane-parallel line-by-line radiative transfer equations and empirical approximations derived from column integrated and surface reference quantities. It is assumed that the atmosphere is entirely composed of N_2 and O_2 gas as well as H_2O vapor and aerosols. Since microwave remote sensing of ocean surfaces generally employs long-wavelength instruments, the scattering contribution of large aerosols is neglected. The top-of-atmosphere (located at s_t) brightness temperature can be computed as a sum of the attenuated emission from the ocean surface, the atmospheric path emission (a function of atmospheric temperature T_{atm}), and the reflected atmosphere and extraterrestrial (T_{sky}) emission

$$T_B = \epsilon T_S e^{-\tau(s_t)} + \int_{\tau(0)}^{\tau(s_t)} T_{atm}(s)e^{-(\tau(s_t) - \tau(s))}d\tau(s)$$
$$+ R\int_{\tau(s_t)}^{\tau(0)} \left(T_{atm}(s) + T_{sky}\right)e^{-\tau(s)}d\tau(s)e^{-\tau(s_t)}. \tag{15}$$

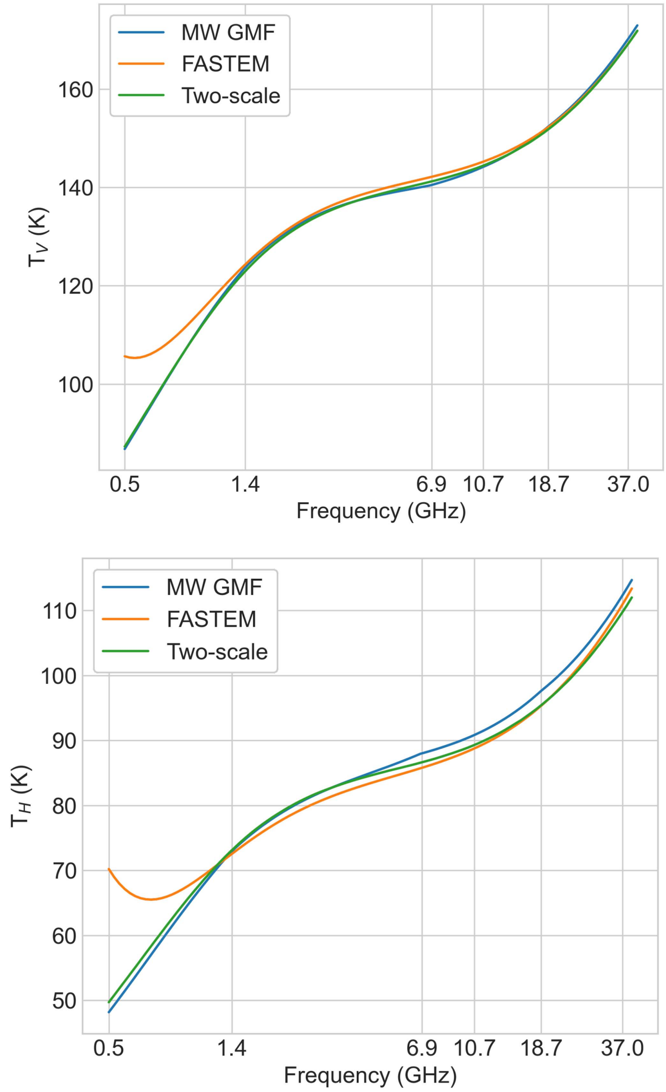

Fig. 5. Upwind brightness temperatures at a 45° incidence angle for a 20 °C, 34 psu ocean surface roughened by a 10 m/s wind using different FOAM surface emission models. The FASTEM model exhibits non-physical behavior when extrapolated lower than 1.4 GHz.

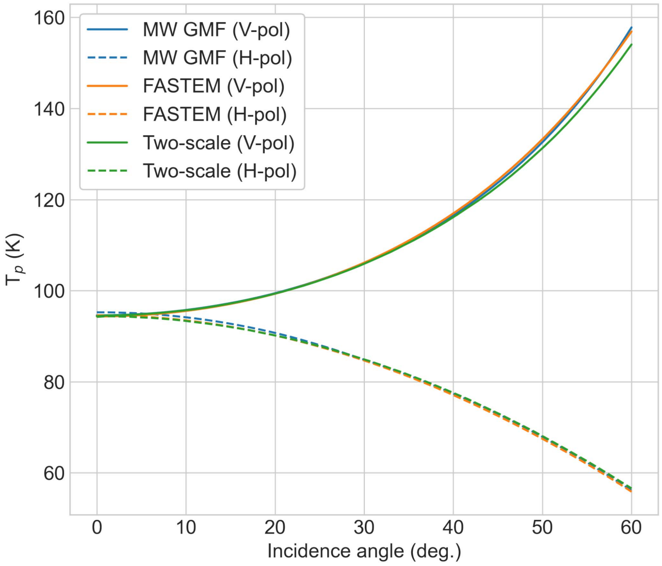

Fig. 6. Upwind brightness temperatures at 1.4 GHz for a 20 °C, 34 psu ocean surface roughened by a 10 m/s as a function of incidence angle.

The atmospheric path opacity τ is the product of the optical path s and the absorptivity of the atmosphere at the location along the path. In the low refraction assumption, the optical path is equivalent to the vertical coordinate times the secant of the incidence angle. We use the propagation model of Rosenkranz [32] to compute the atmospheric absorptivity term (see Fig. 8). Solution of these equations requires that vertical profiles of temperature, pressure, water vapor, and liquid water are provided via ancillary data.

The module also includes a less expensive atmospheric contribution calculation which is based solely on column-integrated quantities (precipitable water vapor V in cm and precipitable liquid water L in mm). We use a model similar to that of Brown et al. [33] with an optional dependence on surface temperature T_S

$$T_B = \epsilon T_S e^{-\tau \sec(\theta)} + \left(1 - e^{-\tau \sec(\theta)}\right) T_{up}^{eff}$$

$$+ R\left(1 - e^{-\tau \sec(\theta)}\right) T_{dn}^{eff} e^{-\tau \sec(\theta)} \quad (16)$$

$$\tau = c_0 + c_1 V + c_2 V^2 + c_3 L + c_4 L^2 + c_5 T_S. \quad (17)$$

The frequency-dependent c_n coefficients for the τ function as well as latitude-dependent upwelling and downwelling effective temperatures T_{up}^{eff} and T_{dn}^{eff} are fit to brightness temperature calculations from 0.5 to 40 GHz with (15) using 3-D MERRA-2 profiles from different seasons, and the resulting calculations of brightness temperature are found to agree well with the full radiative transfer calculations. We note that while the rough-surface emissivity is used to compute the reflected brightness temperature contribution, the current implementation of the code does not incorporate a correction term like that discussed in [16] to account for true rough-surface reflection of the downwelling atmospheric brightness temperature. Such a correction will be implemented in future iterations of our software.

D. *Ionosphere and Sky Modules*

Ionospheric effects on the propagation of microwave radiation are accounted for in FOAM's ionosphere module. The polarization of microwave radiation traversing the ionosphere is changed via Faraday rotation. The corresponding Faraday angle is a function of the ionospheric total electron content (TEC) N in TEC units (10^{16} electrons/m^2), the magnetic field vector $\mathbf{B}$ in nanoteslas, the frequency f in GHz, and the propagation vector $\mathbf{x}$ [34]

$$\phi_f = \frac{1.3549 \times 10^{-5}}{f^2} N(\mathbf{B} \cdot \mathbf{x}). \quad (18)$$

At lower frequencies, the high reflection coefficient of the ocean surface and limited atmospheric attenuation result in a non-negligible contribution of microwave sources beyond the earth's atmosphere to space-borne radiometer measurements of the earth's surface; these sources are implemented in FOAM's

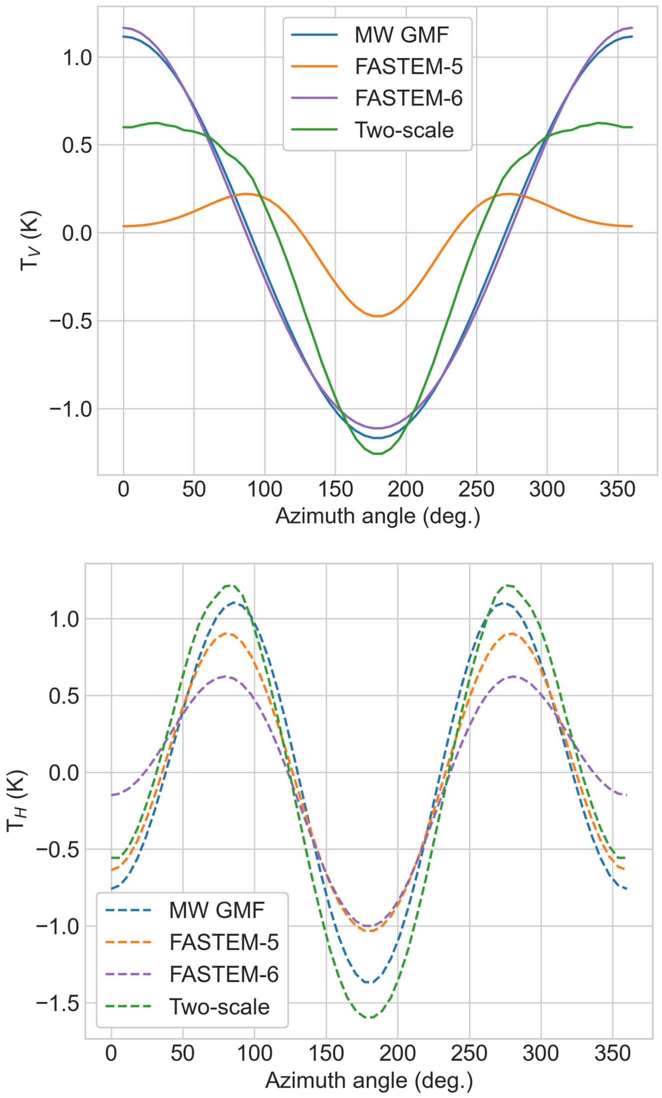

Fig. 7. Brightness temperatures at 19 GHz for a 13 °C, 34 psu ocean surface roughened by a 10 m/s as a function of azimuth angle at an incidence angle of 55°.

sky module. For the contribution of lunar and solar radiation to measured brightness temperature, specular reflection is assumed. This approximation is appropriate for the moon, but may be limited in accuracy for the sun at high elevation angles [35], [36]. The brightness temperature of the Moon is set as constant and equal to the lunar equilibrium temperature of 275 K. The brightness temperature of the sun is modeled with an 11-year period and ranges between 1×10^5 and 5×10^5 K [37]. The contribution of reflected galactic emission is included with modulation due to ocean surface roughness. Wind-roughening of the galactic reflection can be appropriately simulated using a large-scale roughness model [38]. In the local coordinate system, galactic microwave radiation propagates toward earth with a direction vector k_i and the scattered radiation propagates away from earth with a direction vector k_s

$$T_B^{k_s} = \iint \Gamma(k_i, k_s) T_B^{k_i} dk_i^x dk_i^y \tag{19}$$

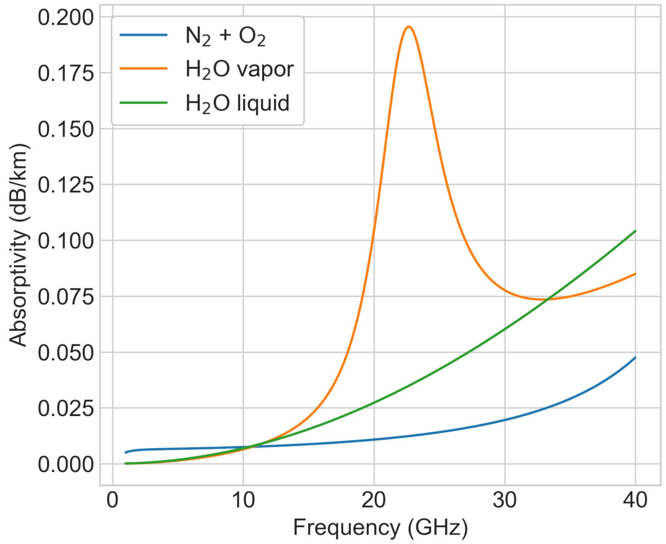

Fig. 8. Atmospheric absorptivity in dB/km assuming 10 °C temperature, 950 mbar pressure, 10 g/m^3 water vapor, and 0.1 g/m^3 liquid water.

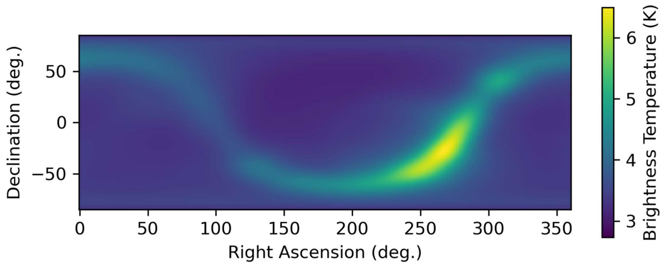

Fig. 9. Roughened galactic background reflection map computed using (19) assuming ocean roughening by a 5 m/s 10-m wind.

$$dk_i^x dk_i^y = \cos\theta d\theta d\phi.$$

The scattering function $\Gamma(k_i, k_s)$ is defined by [38]. The term Υ represents the change of polarization as the dot product of the prereflection polarization vector P^* with the local vertical and horizontal polarization vectors V_s and H_s

$$\Gamma(k_i, k_s) = \frac{P(S_x, S_y)}{4(k_s \cdot z)(k_i \cdot z)} \Upsilon \tag{20}$$

$$\Upsilon = |P_s^* \cdot H_s|^2 |R_H|^2 + |P_s^* \cdot V_s|^2 |R_V|^2 . \tag{21}$$

For satellite missions, these equations need to be evaluated for gridded locations within an orbit at a given sidereal time, which is computationally prohibitive for experimenting with salinity retrieval accuracy with several mission architectures. To approximate this effect, the roughened galactic reflection is calculated for several wind speeds at nadir reflection and stored in tables by right ascension and declination of the nadir reflection. The galactic contribution is then approximated by computing the direction of specular reflection and polarization at run time. The rough-surface galactic reflection intensity is shown for a 5 m/s uniform ocean wind speed in Fig. 9.

E. Ancillary Data

For the forward model mode, FOAM modules require access to ancillary data as a function of latitude, longitude, and time. While users can pass files as input arguments to the various modules in offline mode, FOAM also allows users to access ancillary data from various archive centers via an OpenDAP interface. This functionality is built on top of the xarray package [39]. The ocean module requires ancillary land mask, sea surface temperature, and sea surface salinity maps. FOAM uses the EASE Grid product (which is downloaded and cached on first startup of the program) to mask land and ice-covered ocean regions with 3 km resolution [40]. For sea surface temperature, FOAM provides access to the group for high resolution sea surface temperature (GHRSST) Level 4 products with varying spatial resolutions as processed by various GHRSST member organizations [41]. For salinity, access is provided to multimission optimally interpolated salinity datasets from SMAP, SMOS, and Aquarius [42], as well as individual Level 3 SMAP 8-day or Aquarius 7-day running average products processed by JPL. Additionally, access is provided to HYCOM model outputs, which contain sea surface temperature, salinity, and sea ice fraction fields [43]. The atmosphere module provides access to 2-D surface/column-integrated quantities as well as 3-D atmospheric profiles from GMAO modern-era restrospective analysis version 2 (MERRA-2) [44] and the NCEP/NCAR reanalysis [45]. Available quantities from these products include surface temperature and pressure, 10-m vector winds, and water liquid/vapor abundances. Ionospheric TEC is read into the ionosphere module from GPS-derived ionospheric TEC datasets obtained from the CDDIS DAAC. In addition to the aforementioned ancillary sources, users can also implement their own ancillary data reader subclasses to access data from different sources.

F. Solver Module

FOAM's solver module queries the individual geophysics modules based on the observation tracks generated from a spacecraft object, which include information on the subtended latitude and longitude by each radiometer instrument at a given time as well as the corresponding reflection direction vectors. L1-equivalent noise-free brightness temperatures are computed based on the module objects that are provided to the solver, and the solver brightness temperature routines also return dictionaries of ancillary parameters at each observed location. For L2-equivalent sea state parameter retrievals, the inputs to and outputs from the forward model brightness temperature computations are provided as inputs to the retrieval function, as well as relevant radiometer instrument parameters such as center frequency, bandwidth, and receiver noise (as well as an arbitrary bias option. Based on these parameters, noise is then added to the forward model brightness temperatures prior to the retrieval solution. The number of retrieved parameters is determined from user specification (e.g., only SSS or SSS and SST, etc.) and the joint retrieval of these parameters is conducted using least squares methods implemented by the Scipy package [46].

III. OBSERVING SIMULATIONS

Our intention in the development of the simulator discussed in the previous section was to develop a framework for investigating different mission geometries toward the design of future ocean salinity remote sensing missions. Since the range of possible trades is broad, we limit discussion in this article to two major design choices and their impacts. The first is the impact of increasing radiometer bandwidth on the sensitivity of the retrieved SSS. Broadly, improvements in the sensitivity of radiometer brightness temperature T_B measurements are afforded by increasing the observing bandwidth B, increasing the observing duration τ, or decreasing the noise temperature of the receiver T_r (also written as the noise figure NF)

$$\Delta T = \frac{T_B + T_r}{\sqrt{B\tau}} \tag{22}$$

$$T_r = 290(10^{NF/10} - 1). \tag{23}$$

Thus, increasing the radiometer bandwidth will lead to more accurate measurements of T_B for a given revisit time. As we mentioned previously, limitations in bandwidth for prior *L*-band radiometer instruments are largely driven by spectrum allocation logistics, which can be overcome somewhat by dynamic channel-dependent excision of RFI. It is also desirable to obtain highly accurate snapshot observations to capture mesoscale trends in SSS variability; mesoscale variability in SSS is both broadly interesting in its own right as well as being useful in the development of subscale parameterizations for ocean dynamics in global forecast models. Retrieval of SSS quantities from T_B measurements further rely on scene ancillary information from either models or concurrent measurement. The frequency dependence of these scene contributions to the observed microwave brightness temperature can be used to mitigate uncertainties in their estimates. The desire to determine the frequency dependence of microwave emission from the ocean surface with a wide-bandwidth receiver is synergistic with the need to measure brightness temperature at high spectral resolution to limit data loss due to RFI. In addition to considering the impact of wideband observing systems, we also consider here the employment of targeted revisit geometries oriented toward a specific observation. As the cost of launch continues to decrease for small satellites in the coming years, it may become prudent to design relatively lower cost missions that are focused on studying specific regional ocean processes as opposed to fielding a more costly global observing system. We, therefore, highlight in this section ocean processes traced by SSS which could be measured with comparable or greater quality using targeted revisits.

In this section, we examine a few cases of SSS measurements over regions of broad oceanographic interest and consider how different mission design choices affect the resulting retrieved SSS products. Specifically, we simulate observations of SSS structure in Gulf Stream eddies, Southern Ocean salinity fronts, and Pacific tropical instability waves. In all cases, we use the HYCOM model as the ground-truth ocean state [43].

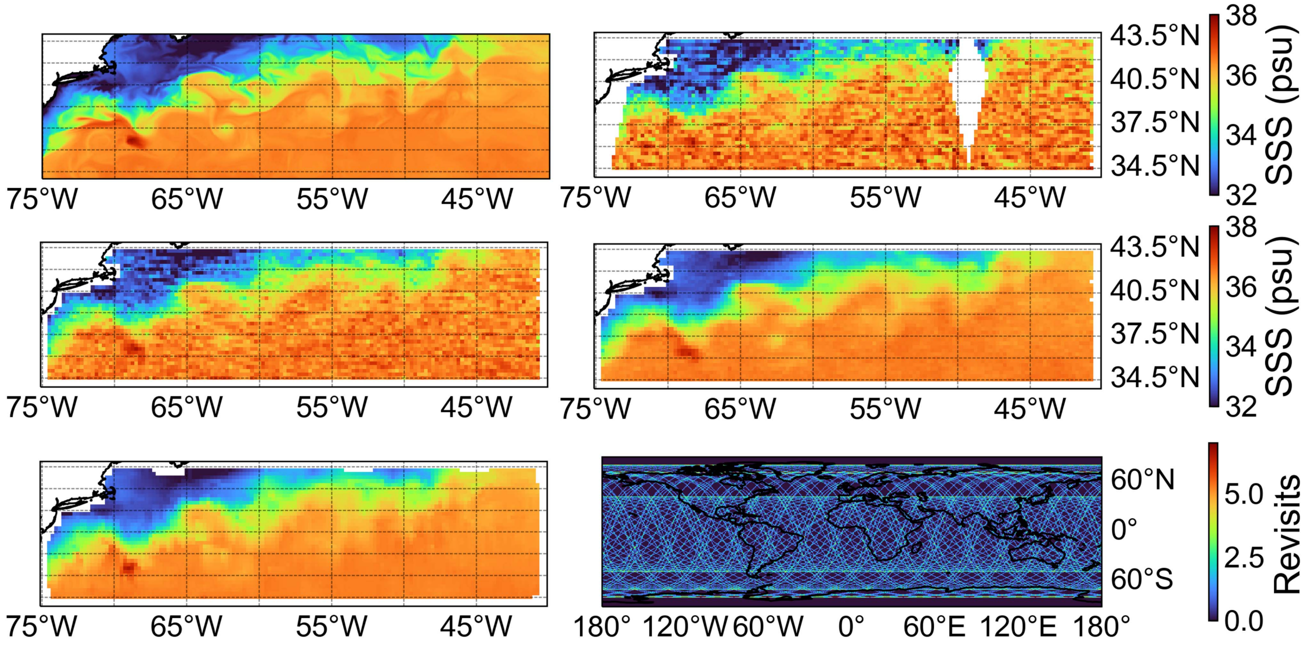

Fig. 10. (Top left) Two-day average SSS field from the HYCOM analysis from May 2020 over the Gulf Stream current. A high salinity eddy feature is apparent at 38 N, 70 W; this eddy forms on May 22 and dissipates by May 24, 2020. Two-day averaged retrievals of SSS over this region are shown for (top right) a SMAP-like architecture (1.4 GHz, $\Delta T = 0.7$ K [49]), (center left) a CIMR-like architecture (1.4, 6.9, 10.6 GHz, $\Delta T = 0.5$ K [2]), (center right) the CIMR architecture with a wideband *L*-band receiver (1.1–1.7, 6.9, 10.6 GHz, $\Delta T = 0.3$ K), and (bottom left) a constellation of three satellites with fixed-pointing radiometers (0.5–2 GHz, Channel $\Delta T = 0.5$ K). The revisit time over earth for the constellation geometry is shown in the bottom right.

A. Observing Gulf Stream Eddy Structure

The Gulf Stream off the coast of the northeast United States forms a boundary between cold, fresh waters supplied from the subpolar North Atlantic Ocean via the Labrador current and the warm, salty waters of the subtropical North Atlantic Ocean. Prior remote SSS observations over this region have characterized the nature of density contrasts and profiled the salinity behavior of cold- and warm-core eddies that pinch off from the Gulf Stream meanders [47], [48]. Accurate characterization of salinity structure associated with Gulf Stream meanders and rings is important to the understanding of the related ocean dynamics, including exchanges between the subpolar and subtropical gyres of the North Atlantic Ocean. We consider here the challenges associated with detecting such eddies with different spacecraft/sensor characteristics. Specifically, we simulate measurements of SSS over a rapidly formed high SSS eddy present in the HYCOM ocean analysis at 38 N, 70 W between May 22–23, 2020, as shown in the top left corner of Fig. 10. We consider four different measurement approaches to detect this feature in the Gulf Stream salinity field: SMAP simulations (1.4 GHz, $B = 27$ MHz, $\text{NF} = 3$ dB, $\Delta T = 0.7$ K [49]), CIMR simulations (1.4, 6.9, 10.6 GHz, *L*-band $B = 27$ MHz, $\text{NF} = 2.5$ dB, $\Delta T = 0.5$ K [2]), CIMR extended (including wideband contribution from NASA) simulations (1.1–1.7, 6.9, 10.6 GHz, L-band channel $B = 100$ MHz, $\text{NF} = 2.5$ dB, $\Delta T = 0.3$ K), and a satellite constellation with wideband, fixed-pointing radiometers (0.5–2 GHz, channel $B = 100$ MHz, $\text{NF} = 3$ dB, $\Delta T = 0.5$ K). For all simulations, the integration time was 28 ms. The constellation includes three satellites orbiting with inclinations of 45°, 75°, and 105°, and the 2-day equivalent revisit over the full globe is shown in the lower right of Fig. 10. The 2-day average retrieved SSS measurements are shown in Fig. 10. As shown in this figure, the mission geometries employing wideband *L*-band receivers have greater capability to detect and characterize the high salinity eddy feature, while the narrowband systems are less capable of resolving this feature given the measurement noise. While the fixed-pointing constellation is not able to achieve as high of spatial resolution as a conical scanner with a larger reflector, the sensitivity of the wideband receiver permits recovery of this mesoscale feature.

B. Southern Ocean Fronts

Measurements of SSS structure associated with the fronts of the Antarctic Circumpolar Current (ACC) in the Southern Ocean are particularly challenging due to the lower sensitivity of *L*-band radiometry to SSS variations over cold waters, the relatively weak SSS variation associated with the ACC fronts, and rapid and variable wind speeds in this region. Fronts in the Southern Ocean are locally defined by sharp gradients in sea-surface properties such as SSS, SST, and sea surface height (SSH) [50]. Front boundaries are constantly shifting, and estimation of vertical and horizontal ocean exchange processes are tied to accurate descriptions of front locations. Due to the lower sensitivity of satellite salinity measurements over colder waters, identification of front boundaries from such measurements is limited to averages over long periods of time. Additionally, different satellite products demonstrate different local and seasonal trends [51]. We consider here the challenge of accurately measuring SSS over the Southern Ocean so that the locations of front boundaries are clearly visible. Our simulations are conducted

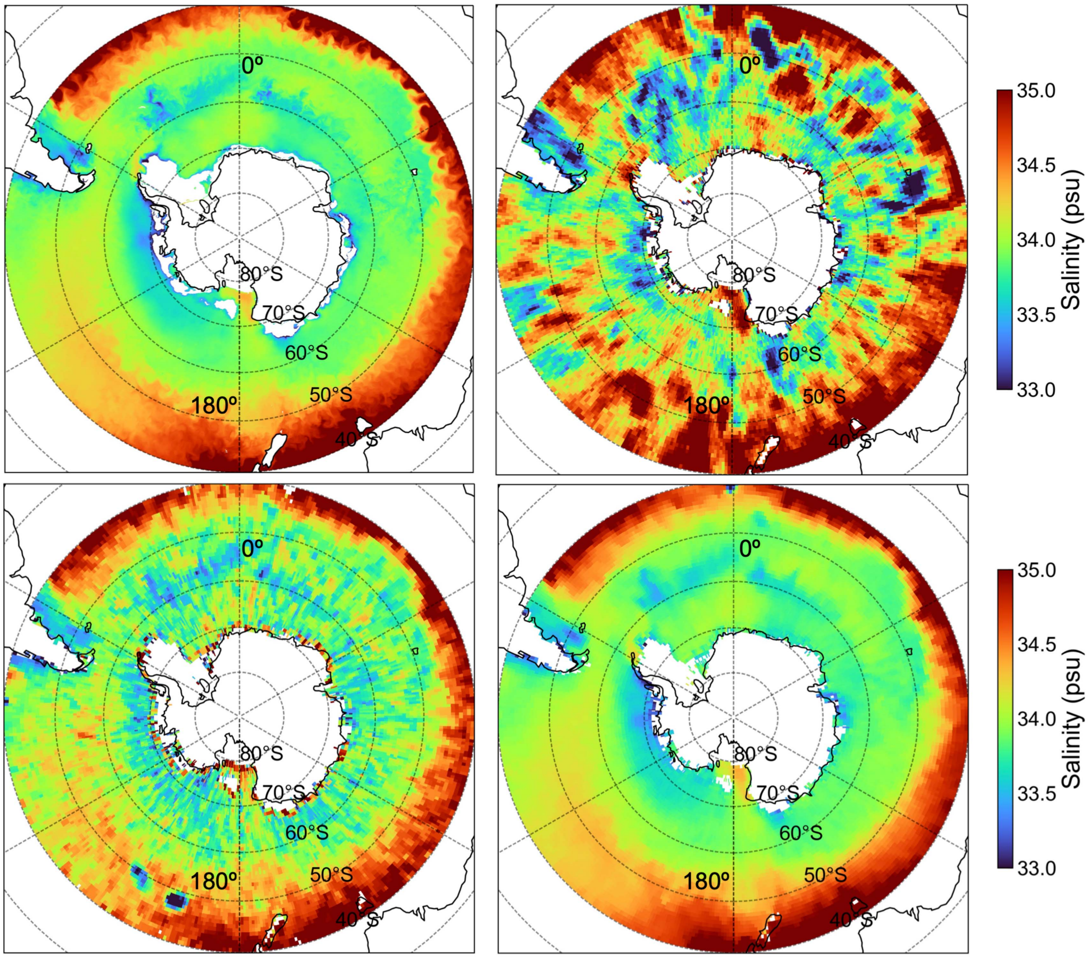

Fig. 11. (Top left) 14-day averaged SSS for the HYCOM model over the Southern Ocean during its summer in February. 14-day averages of retrieved SSS with corrupted ancillary wind field information for (top right) a SMAP-like receiver (1.4 GHz, $\Delta T = 0.7$ K), (bottom left) a CIMR-like receiver (1.4 GHz, 6.9 GHz, 10.7 GHz, $\Delta T = 0.5$ K), and (bottom right) a wideband L-band receiver (0.5–2 GHz, Channel $\Delta T = 0.5$ K). Figures in the bottom row are derived from simultaneous retrieval of OVW and SSS using spectral information outside of 1.4 GHz, mitigating corruption in the ancillary field.

during the southern hemisphere summer in February, where the sea ice has receded and front boundaries are apparent closer to the sheet. To further complicate our retrieval, we introduce a timestep-offset in the ancillary wind data provided to the simulator (from the NCEP analysis). With these corrupted ancillary winds, we then conduct retrievals for a SMAP-like orbital geometry with different receiver characteristics: a narrowband system (1.4 GHz, $\Delta T = 0.7$ K), a more sensitive narrowband system with higher frequencies (e.g., CIMR) (1.4 GHz, 6.9 GHz, 10.7 GHz, $\Delta T = 0.5$ K) and a wideband system (0.5–2 GHz, Channel $\Delta T = 0.5$ K). While the narrowband L-band only system (e.g., SMAP) is fully reliant on the available ancillary wind data, the sensor systems with higher frequencies are capable of simultaneous OVW and SSS retrieval, thereby mitigating the corruption in the ancillary wind data. The results of these retrievals are shown in Fig. 11. While the CIMR-like architecture obtains a higher quality averaged SSS retrieval over the SMAP-like architecture, the wideband system recovers the SSS field with excellent accuracy (even on snapshot scales). SSS fronts are clearly visible in these retrievals, permitting identification of front boundaries with greater accuracy than possible with narrowband L-band receivers.

C. Tropical Instability Wave Spectra

Tropical instability waves and eddy systems form near the boundaries of the equatorial cold tongue in the Pacific ocean due to barotropic and baroclinic instabilities in equatorial current systems [52], [53]. The top of Fig. 12 shows a snapshot of HYCOM analysis tropical instability wave system in the Pacific ocean off the coast of Central America which is our specific region of interest for this section. Previous remote SSS observations have been used to derive the phase speeds of waves within fixed period bands and to assess the relative impact of SSS and SST variations on density gradients [53], [54], [55]. We consider here the challenge of accurately characterizing the power spectrum of the Pacific tropical instability wave system from spacecraft SSS observations, specifically trading revisit time versus snapshot observation sensitivity. Two spacecraft/sensor configurations are compared: an Aquarius-like sensor and an

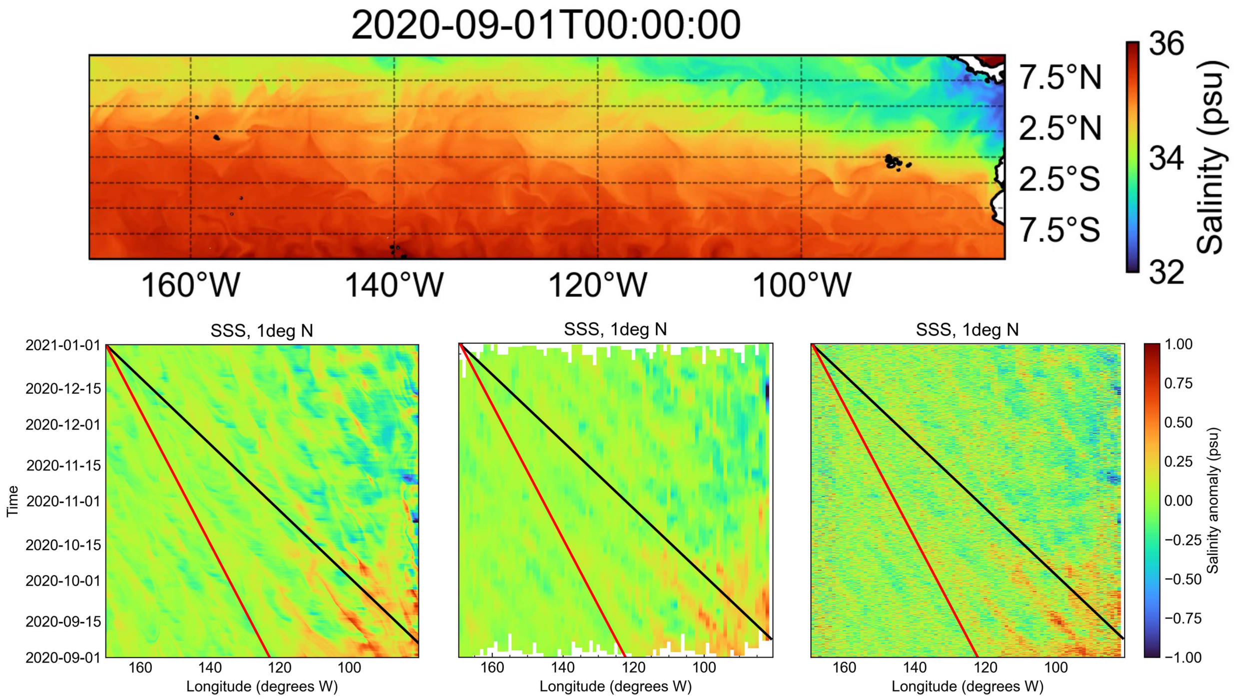

Fig. 12. (Top) HYCOM model SSS within the Pacific equatorial tropical instability wave system corresponding to September 1, 2020. (Bottom) Hovmoller diagrams over four months for (left) the HYCOM model, (center) simulated observations with an Aquarius-like sensor, and (right) simulated observations with an equatorial orbiting conical scanning instrument. The black line corresponds to a wave phase speed of 1 m/s, and the red line corresponds to a wave phase speed of 0.5 m/s.

equatorial-orbiting conical scanner instrument. The Aquarius instrument orbits in a sun-synchronous configuration and features three radiometer horns at look angles between 20° and 50°; the instrument ΔT is specified as 0.15 K [56]. The equatorial orbiter instrument achieves faster revisit, but includes a less sensitive receiver ($\Delta T = 0.5$ K). The bottom row of Fig. 12 shows salinity anomaly (deviation from the mean) Hovmoller diagrams at 1° north over a four month period derived from the HYCOM analysis, interpolated Aquarius-like sensor observations, and equatorial scanning sensor observations. While the equatorial orbiter diagram is significantly noisier, the improved revisit permits resolution of finer scale features. This is confirmed in the longitudinal-averaged power spectral density of the 1° North salinity anomaly time series shown in Fig. 13. While the interpolated Aquarius observations are better able to recover the spectrum within the 0.5 m/s band, the higher revisit equatorial orbiter is able to recover the spectrum for waves which propagate faster. Such simulations could be expanded to determine the necessary receiver sensitivity and/or revisit time necessary to recover wave spectral structure out to an arbitrary frequency within different tropical instability wave systems.

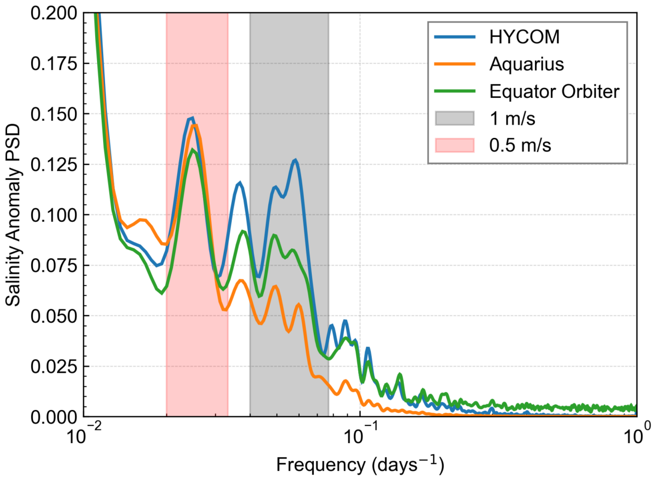

Fig. 13. Power spectral density of the salinity anomalies determined from the longitudinal average of the time series shown in the bottom row of Fig. 12. With higher revisit, the equatorial orbiter is better able to recover the spectrum for faster waves.

D. Discussion

In our observing simulations, we have considered several specific cases in which targeted revisit and wider bandwidth instrument architectures could provide significant improvements in the recovery of SSS trends from satellite measurements. In highly time-variable systems, such as the Gulf Stream and both Atlantic/Pacific tropical instability wave eddy systems, improved snapshot sensitivity from spacecraft measurements can facilitate the adoption of SSS as a regional dynamic tracer. Sensitive SSS measurements in this context can be used as both validation to regional submesoscale dynamical simulations and as an additional degree of freedom in data-driven forecasting of dynamical processes [57], [58]. Accurate study of the connections between ocean salinity and ice melt in cold water systems such as the Arctic and Southern oceans will also become more important as warming continues to impact these regions. It will be imperative for future remote sensing missions to accurately characterize seasonal trends in these regions, and there is evidence to suggest that even considerable time-averages of current spacecraft products are not capable of such characterization [51]. From our case studies, we conclude that wideband and targeted revisit systems are capable of meeting these challenges and broadly improving the state of the art in SSS remote measurement. Similar conclusions have also been reached from recent theoretical sensitivity studies [7], whereas our work supports these conclusions from a practical perspective.

The trade space in design of SSS remote sensing missions from space is broad, and there are many avenues for further research in this area beyond the case studies considered here. With regards to wideband systems, future studies should consider the impact of radio frequency interference over different frequency ranges [6] using source density maps inferred from prior *L*-band missions. While we considered the impact of wind speed errors in this study, a systematic investigation of the impact of biases and errors in all relevant ancillary data fields (particularly ionospheric and galactic components) should also be undertaken to improve error budget estimates. Additionally, the impact of varying spatial resolution with wavelength on the achievable resolution of retrieved SSS using wideband spectrometer systems should also be considered in detail. In addition to the maturation of wideband radiometer systems, advancements in the achievable spatial resolution of SSS remote measurements are also under consideration using interferometer systems [5]. Since improvements in spatial resolution using aperture synthesis techniques impose penalties on snapshot sensitivity, we encourage detailed study of the impact of measurement spatial resolution on the science return of SSS remote sensing missions. Improvements in spatial resolution will be particularly important for resolving processes near coastlines and ice edges, but it will be necessary to balance the spatial resolution achieved with the sensitivity of the retrieved salinity field for future missions. Overall, we encourage further case studies similar to those presented here using the FOAM simulator package over a wider range of both ocean environments and operational capabilities to facilitate the design of next generation SSS observing systems.

IV. CONCLUSION

The continued development and deployment of *L*-band microwave radiometer instruments on future satellite missions will permit continuity in the measurement of SSS and its incorporation into earth system models. In this article, we have presented and described a new open source software package capable of simulating fixed-pointing and scanning microwave radiometer observations of ocean state parameters. We subsequently have applied this software to conduct simulations of satellite SSS missions over selected regions of broad oceanographic interest, demonstrating how the employment of wideband receivers and targeted revisit geometries can lead to improved sensitivity of observing systems to SSS variations from mesoscales and synoptic time scales. These results provide practical demonstration of the capability of next generation wideband radiometer instruments to improve sensitivity in remote sensing of SSS by an order of magnitude, and the inclusion of such instruments in future missions should be a top priority. We encourage future work in the application of this simulator framework to SSS measurements in other high-priority regions (such as the Arctic ocean and coastal oceans) and a more rigorous assessment of trades to ensure that an optimal mission can be designed within a given cost.

REFERENCES

[1] N. Reul et al., “Sea surface salinity estimates from spaceborne l-band radiometers: An overview of the first decade of observation (2010–2019),” *Remote Sens. Environ.*, vol. 242, 2020, Art. no. 111769, doi: 10.1016/j.rse.2020.111769.

[2] L. Kilic et al., “Expected performances of the copernicus imaging microwave radiometer (CIMR) for an all-weather and high spatial resolution estimation of ocean and sea ice parameters,” *J. Geophysical Res.: Oceans*, vol. 123, pp. 7564–7580, 2018.

[3] Y. Li, X. Yin, W. Zhou, M. Lin, H. Liu, and Y. Li, “Performance simulation of the payload IMR and MICAP onboard the chinese ocean salinity satellite,” *IEEE Trans. Geosci. Remote Sens.*, vol. 60, 2022 Art. no. 5301916, doi: 10.1109/TGRS.2021.3111026.

[4] W. Tang et al., “The potential and challenges of using soil moisture active passive (SMAP) sea surface salinity to monitor arctic ocean freshwater changes,” *Remote Sens.*, vol. 10, 2018, Art. no. 869.

[5] N. J. Rodriguez-Fernandez et al., “SMOS-HR: A high resolution l-band passive radiometer for earth science and applications,” in *Proc. Int. Geosci. Remote Sens. Symp.*, 2019, pp. 8392–8395.

[6] J. T. Johnson et al., “Microwave radiometry at frequencies from 500 to 1400 MHz: An emerging technology for earth observations,” *IEEE J. Sel. Topics Appl. Earth Observ. Remote Sens.*, vol. 14, pp. 4894–4914, 2021, doi: 10.1109/JSTARS.2021.3073286.

[7] D. M. L. Vine and E. P. Dinnat, “Measurement of SST and SSS using frequencies in the range 0.3–2.0 GHz,” *Radio Sci.*, vol. 57, Apr. 2022, Art. no. e2021RS007415. [Online]. Available: https://onlinelibrary.wiley.com/doi/10.1029/2021RS007415

[8] J. T. Johnson et al., “Real-time detection and filtering of radio frequency interference onboard a spaceborne microwave radiometer: The CubeRRT mission,” *IEEE J. Sel. Topics Appl. Earth Observ. Remote Sens.*, vol. 13, pp. 1610–1624, 2020, doi: 10.1109/JSTARS.2020.2978016.

[9] C. Acton, N. Bachman, B. Semenov, and E. Wright, “A look towards the future in the handling of space science mission geometry,” *Planet. Space Sci.*, vol. 150, pp. 9–12, 2018, doi: 10.1016/j.pss.2017.02.013.

[10] A. Annex et al., “SpiceyPy: A pythonic wrapper for the spice toolkit,” *J. Open Source Softw.*, vol. 5, 2020, Art. no. 2050.

[11] F. Ulaby and D. Long, *Microwave Radar and Radiometric Remote Sensing*, 1st ed. Ann Arbor, MI, USA: Univ. Michigan Press, 2014.

[12] L. Klein and C. Swift, “An improved model for the dielectric constant of sea water at microwave frequencies,” *IEEE J. Ocean. Eng.*, vol. 2, no. 1, pp. 104–111, Jan. 1977. [Online]. Available: https://ieeexplore.ieee.org/document/1145319/

[13] W. Ellison et al., “New permittivity measurements of seawater,” *Radio Sci.*, vol. 33, pp. 639–648, May 1998. [Online]. Available: https://doi.wiley.com/10.1029/97RS02223

[14] Y. Zhou, R. H. Lang, E. P. Dinnat, and D. M. L. Vine, “Seawater debye model function at l-band and its impact on salinity retrieval from aquarius satellite data,” *IEEE Trans. Geosci. Remote Sens.*, vol. 59, no. 10, pp. 8103–8116, Oct. 2021.

[15] T. Meissner and F. J. Wentz, “The complex dielectric constant of pure and sea water from microwave satellite observations,” *IEEE Trans. Geosci. Remote Sens.*, vol. 42, no. 9, pp. 1836–1849, Sep. 2004.

[16] T. Meissner and F. J. Wentz, “The emissivity of the ocean surface between 6 and 90 GHz over a large range of wind speeds and earth incidence angles,” *IEEE Trans. Geosci. Remote Sens.*, vol. 50, no. 8, pp. 3004–3026, Aug. 2012. [Online]. Available: https://ieeexplore.ieee.org/document/6145646/

[17] J. Boutin et al., "Correcting sea surface temperature spurious effects in salinity retrieved from spaceborne l-band radiometer measurements," *IEEE Trans. Geosci. Remote Sens.*, vol. 59, no. 9, pp. 7256–7269, Sep. 2021.

[18] T. Meissner, F. J. Wentz, and L. Ricciardulli, "The emission and scattering of l-band microwave radiation from rough ocean surfaces and wind speed measurements from the aquarius sensor," *J. Geophysical Res.: Oceans*, vol. 119, pp. 6499–6522, Sep. 2014. [Online]. Available: https://doi.wiley.com/10.1002/2014JC009837

[19] S. H. Yueh et al., "L-band passive and active microwave geophysical model functions of ocean surface winds and applications to aquarius retrieval," *IEEE Trans. Geosci. Remote Sens.*, vol. 51, no. 9, pp. 4619–4632, Sep. 2013. [Online]. Available: https://ieeexplore.ieee.org/document/6553597/

[20] S. Yueh, "Modeling of wind direction signals in polarimetric sea surface brightness temperatures," *IEEE Trans. Geosci. Remote Sens.*, vol. 35, no. 6, pp. 1400–1418, Nov. 1997. [Online]. Available: https://ieeexplore.ieee.org/document/649793/

[21] P. Janssen, *The Interaction of Ocean Waves and Wind*. Cambridge, U.K.: Cambridge Univ. Press, Oct. 2004. [Online]. Available: https://www.cambridge.org/core/product/identifier/9780511525018/type/book

[22] P. A. Hwang, Y. Fan, F. J. Ocampo-Torres, and H. García-Nava, "Ocean surface wave spectra inside tropical cyclones," *J. Phys. Oceanogr.*, vol. 47, pp. 2393–2417, 2017.

[23] S. Durden and J. Vesecky, "A physical radar cross-section model for a wind-driven sea with swell," *IEEE J. Ocean. Eng.*, vol. 10, no. 4, pp. 445–451, Oct. 1985. [Online]. Available: https://ieeexplore.ieee.org/document/1145133/

[24] A. Fung and K. Lee, "A semi-empirical sea-spectrum model for scattering coefficient estimation," *IEEE J. Ocean. Eng.*, vol. 7, no. 4, pp. 166–176, Oct. 1982. [Online]. Available: https://ieeexplore.ieee.org/document/1145535/

[25] P. A. Hwang, "Foam and roughness effects on passive microwave remote sensing of the ocean," *IEEE Trans. Geosci. Remote Sens.*, vol. 50, no. 8, pp. 2978–2985, Aug. 2012.

[26] M. D. Anguelova, "Complex dielectric constant of sea foam at microwave frequencies," *J. Geophysical Res.: Oceans*, vol. 113, pp. 1–22, 2008.

[27] A. Stogryn, "The emissivity of sea foam at microwave frequencies," *J. Geophysical Res.*, vol. 77, pp. 1658–1666, 1972.

[28] S. H. Yueh, R. Kwok, F. K. Li, S. V. Nghiem, W. J. Wilson, and J. A. Kong, "Polarimetric passive remote sensing of ocean wind vectors," *Radio Sci.*, vol. 29, pp. 799–814, Jul. 1994. [Online]. Available: https://doi.wiley.com/10.1029/94RS00450

[29] J. T. Johnson and M. Zhang, "Theoretical study of the small slope approximation for ocean polarimetric thermal emission," *IEEE Trans. Geosci. Remote Sens.*, vol. 37, no. 5, pp. 2305–2316, Sep. 1999.

[30] J. T. Johnson, "An efficient two-scale model for the computation of thermal emission and atmospheric reflection from the sea surface," *IEEE Trans. Geosci. Remote Sens.*, vol. 44, no. 3, pp. 560–568, Mar. 2006.

[31] M. Kazumori and S. J. English, "Use of the ocean surface wind direction signal in microwave radiance assimilation," *Quart. J. Roy. Meteorological Soc.*, vol. 141, pp. 1354–1375, 2015.

[32] P. W. Rosenkranz, "Line-by-line microwave radiative transfer (non-scattering)," *IEEE GRSS Remote Sens. Code Library*, 2019, doi: 10.21982/M81013.

[33] S. T. Brown, C. S. Ruf, and D. R. Lyzenga, "An emissivity-based wind vector retrieval algorithm for the windsat polarimetric radiometer," *IEEE Trans. Geosci. Remote Sens.*, vol. 44, no. 3, pp. 611–621, Mar. 2006.

[34] S. H. Yueh, "Estimates of faraday rotation with passive microwave polarimetry for microwave remote sensing of earth surfaces," *IEEE Trans. Geosci. Remote Sens.*, vol. 38, no. 5, pp. 2434–2438, Sep. 2000.

[35] E. P. Dinnat and D. M. L. Vine, "Impact of sun glint on salinity remote sensing: An example with the aquarius radiometer," *IEEE Trans. Geosci. Remote Sens.*, vol. 46, no. 10, pp. 3137–3150, Oct. 2008.

[36] E. P. Dinnat, S. Abraham, D. M. L. Vine, P. D. Matthaeis, and D. Jacob, "Effect of emission from the moon on remote sensing of sea surface salinity: An example with the aquarius radiometer," *IEEE Geosci. Remote Sens. Lett.*, vol. 6, no. 2, pp. 239–243, Apr. 2009.

[37] C. Ho, S. Slobin, A. Kantak, and S. Asmar, "Solar brightness temperature and corresponding antenna noise temperature at microwave frequencies," Interplanetary Network Progress Report, vol. 42-175, pp. 1–11, Nov. 15, 2008. [Online]. Available: https://ipnpr.jpl.nasa.gov/progress_report/42-175/175E.pdf

[38] T. Meissner, F. Wentz, and D. L. Vine, "Aquarius salinity retrieval algorithm: End of mission algorithm theoretical basis document (ATBD)," Tech. Rep. 120117, 2017. [Online]. Available: https://podaac-tools.jpl.nasa.gov/drive/files/allData/aquarius/docs/v5/AQ-014-PS-0017_Aquarius_ATBD-EndOfMission.pdf

[39] S. Hoyer and J. J. Hamman, "xarray: N-D labeled arrays and datasets in python," *J. Open Res. Softw.*, vol. 5, pp. 1–6, 2017.

[40] M. J. Brodzik, B. Billingsley, T. Haran, B. Raup, and M. H. Savoie, "EASE-grid 2.0: Incremental but significant improvements for earth-gridded data sets," *ISPRS Int. J. Geo-Inf.*, vol. 1, pp. 32–45, 2012.

[41] M. Martin et al., "Group for high resolution sea surface temperature (GHRSST) analysis fields inter-comparisons. Part 1: A ghrsst multi-product ensemble (GMPE)," in *Deep Sea Res. Part II: Top. Stud. Oceanogr.*, vol. 77/80, pp. 21–30, Nov. 2012, doi: 10.1016/j.dsr2.2012.04.013. [Online]. Available: https://linkinghub.elsevier.com/retrieve/pii/S0967064512000616

[42] O. Melnichenko, P. Hacker, N. Maximenko, G. Lagerloef, and J. Potemra, "Optimum interpolation analysis of aquarius sea surface salinity," *J. Geophysical Res.: Oceans*, vol. 121, pp. 602–616, Jan. 2016. [Online]. Available: https://onlinelibrary.wiley.com/doi/abs/10.1002/2015JC011343

[43] E. J. Metzger et al., "Us navy operational global ocean and arctic ice prediction systems," *Oceanogr.*, vol. 27, pp. 32–43, Sep. 2014. [Online]. Available: https://tos.org/oceanography/article/us-navy-operational-global-ocean-and-arctic-ice-prediction-systems

[44] R. Gelaro et al., "The modern-era retrospective analysis for research and applications, version 2 (MERRA-2)," *J. Climate*, vol. 30, pp. 5419–5454, 2017.

[45] E. Kalnay et al., "The NCEP/NCAR 40-year reanalysis project," *Bull. Amer. Meteorological Soc.*, vol. 77, pp. 437–471, Mar. 1996.

[46] P. Virtanen et al., "Scipy 1.0: Fundamental algorithms for scientific computing in python," *Nature Methods*, vol. 17, pp. 261–272, 2020.

[47] N. Reul, B. Chapron, T. Lee, C. Donlon, J. Boutin, and G. Alory, "Sea surface salinity structure of the meandering gulf stream revealed by SMOS sensor," *Geophysical Res. Lett.*, vol. 41, pp. 3141–3148, May 2014. [Online]. Available: https://doi.wiley.com/10.1002/2014GL059215

[48] M. Umbert et al., "Detecting the surface salinity signature of gulf stream cold-core rings in aquarius synergistic products," *J. Geophysical Res.: Oceans*, vol. 120, pp. 859–874, Feb. 2015. [Online]. Available: https://doi.wiley.com/10.1002/2014JC010466

[49] J. R. Piepmeier et al., "SMAP L-band microwave radiometer: Instrument design and first year on orbit," *IEEE Trans. Geosci. Remote Sens.*, vol. 55, no. 4, pp. 1954–1966, Apr. 2017.

[50] C. C. Chapman, M.-A. Lea, A. Meyer, J.-B. Sallée, and M. Hindell, "Defining southern ocean fronts and their influence on biological and physical processes in a changing climate," *Nature Climate Change*, vol. 10, pp. 209–219, Mar. 2020. [Online]. Available: https://www.nature.com/articles/s41558-020-0705-4

[51] C. Garcia-Eidell, J. C. Comiso, E. Dinnat, and L. Brucker, "Sea surface salinity distribution in the southern ocean as observed from space," *J. Geophysical Res.: Oceans*, vol. 124, pp. 3186–3205, 2019.

[52] C. S. Willett, R. R. Leben, and M. F. Lavín, "Eddies and tropical instability waves in the eastern tropical pacific: A review," *Prog. Oceanogr.*, vol. 69, pp. 218–238, 2006.

[53] T. Lee, G. Lagerloef, M. M. Gierach, H. Y. Kao, S. Yueh, and K. Dohan, "Aquarius reveals salinity structure of tropical instability waves," *Geophysical Res. Lett.*, vol. 39, pp. 1–6, 2012.

[54] T. Lee, G. Lagerloef, H. Y. Kao, M. J. McPhaden, J. Willis, and M. M. Gierach, "The influence of salinity on tropical atlantic instability waves," *J. Geophysical Res.: Oceans*, vol. 119, pp. 8375–8394, 2014.

[55] L. Olivier, G. Reverdin, A. Hasson, and J. Boutin, "Tropical instability waves in the atlantic ocean: Investigating the relative role of sea surface salinity and temperature from 2010 to 2018," *J. Geophysical Res.: Oceans*, vol. 125, pp. 1–17, 2020.

[56] J. R. Piepmeier, L. Hong, and F. A. Pellerano, "Aquarius l-band microwave radiometer: 3 years of radiometric performance and systematic effects," *IEEE J. Sel. Topics Appl. Earth Observ. Remote Sens.*, vol. 8, no. 12, pp. 5416–5423, Dec. 2015.

[57] J. A. Mensa, Z. Garraffo, A. Griffa, T. M. Özgökmen, A. Haza, and M. Veneziani, "Seasonality of the submesoscale dynamics in the gulf stream region," *Ocean Dyn.*, vol. 63, pp. 923–941, 2013.

[58] G. Zheng, X. Li, R. H. Zhang, and B. Liu, "Purely satellite data-driven deep learning forecast of complicated tropical instability waves," *Sci. Adv.*, vol. 6, 2020, Art. no. eaba1482.

Alexander Akins (Member, IEEE) received the B.S., M.S., and Ph.D. degrees in electrical and computer engineering from the Georgia Institute of Technology, Atlanta, GA, USA, in 2016, 2018, and 2020, respectively.

He is currently a Staff Member of the Microwave Instrument Science Group, Jet Propulsion Laboratory, California Institute of Technology, Pasadena, CA, USA. His research interests include instrument concept design and radiative transfer modeling for satellite missions measuring sea surface and ice sheet state variables. Outside of Earth science, he is active in solar system radio astronomy, with a specific interest in remote sensing of planetary atmospheres using ground-based microwave and millimeter radio observatories, orbital microwave radiometers, and radio occultation measurements.

Shannon Brown (Senior Member, IEEE) received the B.S. degree in meteorology from Pennsylvania State University, State College, PA, USA, in 2001, and the M.S. degree in atmospheric science, and the Ph.D. degree in geoscience and remote sensing from the University of Michigan, Ann Arbor, MI, USA, in 2003 and 2005, respectively.

He joined Microwave Advanced Systems Section, Jet Propulsion Laboratory (JPL), Pasadena, CA, USA, in 2005, as a Member. He is a Principal Technologist with NASA JPL. He has been involved in the spaceborne Topex; Jason-1, 2, and 3 Microwave Radiometers; and the WindSat Polarimetric Radiometer. He is a Principal Investigator of the Compact Ocean Wind Vector Radiometer being developed for the U.S. Air Force and an Instrumental Scientist for the NASA Juno Microwave Radiometer on the Juno New Frontiers mission to Jupiter. He is a Member of the Ocean Surface Topography Science Team, the Ocean Salinity Science Team, the SMAP Science Team, and the Juno Science Team. His research interests include microwave radiometer system development, calibration, geophysical algorithm development for both passive and active sensors, extraction of climate data records, and radiometer science.

Dr. Brown was a recipient of the NASA Exceptional Achievement Medal in 2009, the JPL Lew Allen Award in 2010, eight NASA group achievement awards, and the NASA Space Act Award in 2012.

Tong Lee received the Ph.D. degree in physical oceanography from the University of Rhode Island, Kingston, RI, USA, in 1994.

After completing his postdoctoral research with the Massachusetts Institute of Technology, Cambridge, MA, USA, in 1994-1996, he became a Scientist of the Jet Propulsion Laboratory (JPL), Pasadena, CA, USA, in late 1996. He was the Supervisor of JPL's Ocean and Ice Group during 2011–2015 and that of the Ocean Circulation and Air-Sea Interaction Group during 2016–2021. He was the Project Scientist for NASA's Aquarius satellite mission during 2013–2017. He is currently a JPL Senior Research Scientist and the lead of NASA's Ocean Salinity Science Team.

Dr. Lee was the recipient of the NASA Exceptional Achievement Medal in 2010, NASA Exceptional Scientific Achievement Medal in 2012 and 2020, and JPL Ed Stone Award for Outstanding Research Publication in 2020.

Sidharth Misra (Senior Member, IEEE) received the B.E. degree in electronics and communication engineering from Gujarat University, Ahmedabad, India, in 2004, the M.S. degree in electrical engineering and computer science from the University of Michigan, Ann Arbor, MI, USA, in 2006, and the Ph.D. degree in atmospheric and space sciences from the Department of Atmospheric, Oceanic and Space Sciences, University of Michigan, in 2011.

He joined JPL in 2011 as a Member of the Microwave Systems Technology Group. He was a Research Engineer with the Space Physics Research Laboratory, University of Michigan, and a Research Assistant with the Danish National Space Center, Technical University of Denmark (DTU), Lyngby, Denmark. He was also with the Space Applications Center, Indian Space Research Organization, Ahmedabad, India. He is currently a Technologist with the NASA Jet Propulsion Laboratory, Pasadena, CA, USA. His research interests include radio frequency interference algorithm development and mitigation, microwave radiometer system development and calibration. He was on the calibration team of the Aquarius radiometer and was the Instrument Scientist on the RACE Mission. He was also the digital back-end lead for the CubeRRT Mission. He is currently on the science team of SMAP, as well as Ocean Vector Winds for the COWVR Mission, and the Radiometer Calibration Team Member for the Juno microwave radiometer. He is the Instrument Manager for the PALS Airborne System, and an Instrument Scientist for the EZIE Mission.

Dr. Misra is a Member of the Advisory Committee for the IEEE Geoscience and Remote Sensing Society (GRSS). He was a recipient of the IGARSS 2006 Symposium Prize Paper Award, the 2009 IEEE-GRSS Mikio Takagi Award, and the 2012 IEEE TGRS Best Reviewer Award. He received the JPL Charles Elachi Early Career Award in 2016, the NASA Early Career Award in 2017, the NASA Technical Achievement Award in 2019, and the JPL Lew Allen Award in 2020. He has also received five NASA Group Achievement Awards. He is an Associate Editor for the GeoScience and Remote Sensing Letters.

Simon Yueh (Fellow, IEEE) received the Ph.D. degree in electrical engineering from the Massachusetts Institute of Technology, Cambridge, MA, USA, in 1991.

From February to August 1991, he was a Postdoctoral Research Associate with the Massachusetts Institute of Technology. In September 1991, he joined the Radar Science and Engineering Section, Jet Propulsion Laboratory (JPL), and has assumed various engineering and science management responsibilities. He was the Project Scientist of the National Aeronautics and Space Administration (NASA) Aquarius mission from January 2012 to September 2013, the Deputy Project Scientist of NASA Soil Moisture Active Passive Mission from January 2013 to September 2013, and has been the SMAP Project Scientist since October 2013. He has been the Principal/Co-Investigator of numerous NASA and DOD research projects on remote sensing of ocean salinity, ocean wind, terrestrial snow, and soil moisture. He has authored four book chapters, and authored or coauthored more than 200 publications and presentations.

Dr. Yueh was the recipient of the 1995 IEEE GRSS Transaction Prize Paper Award for a paper on polarimetric radiometry, JPL Lew Allen Award in 1998, the 2000 Best Paper Award in the IEEE International Geoscience and Remote Symposium 2000, 2002 IEEE GRSS Transaction Prize Paper Award, JPL Ed Stone Award in 2003, 2010 IEEE GRSS Transaction Prize Paper Award, 2014 IEEE GRSS Transaction Prize Paper Award, NASA Exceptional Technology Achievement Award in 2014 and NASA Outstanding Public Leadership Medal in 2017, and 2021 IEEE GRSS J-STARS Prize Paper Award. He was an Associate Editor for *Radio Science* from 2003 to 2007, and was the Editor-in-Chief of IEEE TRANSACTIONS OF GEOSCIENCE AND REMOTE SENSING from 2018 to 2022. He is a Member of the American Geophysical Union and URSI Commission F.